



Article

How Groundwater Level Fluctuations and Geotechnical Properties Lead to Asymmetric Subsidence: A PSInSAR Analysis of Land Deformation over a Transit Corridor in the Los Angeles Metropolitan Area

Mohammad Khorrami ^{1,*}, Babak Alizadeh ², Erfan Ghasemi Tousi ³, Mahyar Shakerian ¹, Yasser Maghsoudi ⁴ and Peyman Rahgozar ⁵

¹ Department of Civil Engineering, Faculty of Engineering, Ferdowsi University of Mashhad, Mashhad 91779, Iran; mahyar.shakerian@gmail.com

² Department of Civil Engineering, University of Texas at Arlington, Arlington, TX 76019, USA; babak.alizadeh@mavs.uta.edu

³ Department of Civil and Architectural Engineering and Mechanics, University of Arizona, Tucson, AZ 85721, USA; erfang@email.arizona.edu

⁴ Department of Photogrammetry and Remote Sensing, Faculty of Geodesy and Geomatics Engineering, K. N. Toosi University of Technology, Tehran 19967, Iran; ymaghsoudi@kntu.ac.ir

⁵ M. E. Rinker, Sr. School of Construction Management, University of Florida, P.O. Box 115703, Gainesville, FL 32611, USA; peymanrahgozar@ufl.edu

* Correspondence: mohammad.khorrami@mail.um.ac.ir

Received: 31 December 2018; Accepted: 9 February 2019; Published: 12 February 2019



Abstract: Los Angeles has experienced ground deformations during the past decades. These ground displacements can be destructive for infrastructure and can reduce the land capacity for groundwater storage. Therefore, this paper seeks to evaluate the existing ground displacement patterns along a new metro tunnel in Los Angeles, known as the Sepulveda Transit Corridor. The goal is to find the most crucial areas suffering from subsidence or uplift and to enhance the previous reports in this metropolitan area. For this purpose, we applied a Persistent Scatterer Interferometric Synthetic Aperture Radar using 29 Sentinel-1A acquisitions from June 2017 to May 2018 to estimate the deformation rate. The assessment procedure demonstrated a high rate of subsidence in the Inglewood field that is near the study area of the Sepulveda Transit Corridor with a maximum deformation rate of 30 mm/yr. Finally, data derived from in situ instruments as groundwater level variations, GPS observations, and soil properties were collected and analyzed to interpret the results. Investigation of geotechnical boreholes indicates layers of fine-grained soils in some parts of the area and this observation confirms the necessity of more detailed geotechnical investigations for future constructions in the region. Results of investigating line-of-sight displacement rates showed asymmetric subsidence along the corridor and hence we proposed a new framework to evaluate the asymmetric subsidence index that can help the designers and decision makers of the project to consider solutions to control the current subsidence.

Keywords: subsidence monitoring; persistent scatterer interferometry; asymmetric subsidence; groundwater level variation; Sepulveda Transit Corridor; Los Angeles

1. Introduction

Ground subsidence is mainly due to fluid overexploitation and expanding construction [1–4]. There are several cities and regions suffering from land subsidence, such as Mexico City [5,6], Shanghai, China [7–9], Lhokseumawe, Medan, Jakarta, Bandung, Blanakan, Pekalongan, Bungbulang, and Semarang, Indonesia [10–13], Ravenna, Prato, Bologna, Italy [14–18], Tehran, Rafsanjan, Neyshabour, Mashhad, Iran [19–25], Los Angeles, United States [26–32], and many more places around the world. In the present study, we studied land deformation in Los Angeles metropolitan area, Southern California, with a focus on the study area of a new transit corridor, known as Sepulveda Transit Corridor. This investigation is crucial because land displacement will affect the design and depth of a tunnel [33–36] and should be assessed based on soil properties. Also, all the information about the location, soil and groundwater needs to be carefully managed, analyzed and investigated in planning and design phase of the road construction to ensure the reliability of the subgrade [37–39]. Based on the previous researches in Los Angeles [26–31,40], the ground displacements in this area are mainly due to the groundwater level variations and oil extraction [26].

Advances in technology and science have made accurate measurement of ground deformation simple. Interferometric Synthetic Aperture Radar (InSAR) technique is a geodetic tool to image ground displacement in centimeter-scale and can be a very helpful technique in understanding the earthquakes, volcanos and glaciers [41]. InSAR can also benefit geomorphologists and hydrologist by providing an accurate measurement of slope motion, sediment erosion and deposition, water level fluctuation and soil moisture content [42–46]. InSAR has been considered as a powerful method to monitor ground surface deformations [47] and is an alternative technique to measure surface displacement. InSAR can measure small surface deformations in different situations and projects such as ground settlement and excavations [48]. Using the high spatial and temporal resolution of radar images, the InSAR technique can provide reliable results in the application of subsidence monitoring of such infrastructures as roads [49], subways, rails, and tunnels. Tunnels are visible because of localized subsidence of the above ground surface along their tunnel path. It means that it is possible to determine the effect of tunnel excavation on the ground surface. Highways, standing over the ground surface, in most cases show reliable stability compared to the surrounding areas [50].

A number of studies have used geodetic and InSAR techniques to evaluate the ground deformation in Los Angeles Basin. For example, the radar data acquired by the European Remote Sensing Satellites (ERS-1 and ERS-2) from 1992 to 1999 were analyzed [51] using InSAR to study the ground deformations along the southern San Andreas fault system. In addition, the interseismic crustal movement was measured [52] near Los Angeles, along the San Andreas Fault (SAF), by a new technique for integrating InSAR analysis on ERS descending and ALOS ascending radar images, and GPS data. The outputs display the vertical velocity of land deformation between -2 to $+2$ mm/yr, and shows uplift on the SAF in the Los Angeles area. Several researchers investigated the ground displacements related to groundwater level changes and fluid extraction in the Los Angeles Basin. For instance, radar images of ERS-1/2 satellite and GPS data were deployed [29] to infer the seasonal land deformations related to groundwater extraction in the Los Angeles basin. Also, a study on metropolitan Los Angeles [40] evaluated seasonal oscillations of the Santa Ana aquifer (uplift and subsidence), located in Los Angeles Basin, using InSAR technique from 1998 to 1999. The analysis provided estimates of ground displacement in the Line of Sight (LOS) of the European Remote Sensing (ERS) satellite in the time between satellite passes. The InSAR outputs showed uplift and subsidence in metropolitan Los Angeles to in response to extraction of fluid resources.

The subsidence associated with groundwater pumping and faulting in Santa Ana basin, CA was measured using InSAR technique from 1997 to 1999 and GPS data from 1999 to 2000 [53]. The results showed subsidence as high as 12 mm/yr is happening by groundwater withdrawal and re-injection in metropolitan Los Angeles. A time series analysis of ground deformation by InSAR based on small baseline subset (SBAS) algorithm was carried out [28] for Santa Ana basin in Los Angeles metropolitan area. ERS satellite data from 1995 to 2002 were used and it was found that ground deformations time

series from InSAR significantly agree with GPS time series from Southern California Integrated GPS Network (SCIGN). A temporarily coherent point InSAR method [30] was applied on the Los Angeles Basin, using 32 ERS-1/2 images acquired during 1995 to 2000 to detect land subsidence. InSAR and GPS measurements were used [26] for detecting ground deformations caused by injection of groundwater and oil in Los Angeles from 2003 to 2007. A dataset of 64 TerraSAR-X images has been processed [27] in Los Angeles in the period 2010–2014 and showed a cumulative displacement of -50 mm in oil extraction fields. In 2018, a research [54] conducted to quantify ground deformation in the Los Angeles Basin due to groundwater withdrawal and showed -20 to $+10$ mm/yr LOS displacement rate.

A number of studies have been carried out to measure surface deformation along the transit corridors and their near infrastructures such as aqueducts and levees in California [55,56] and Rome (Italy) [57]. For instance, land subsidence rate of Hampton Roads in Virginia, USA, was estimated [58] using GPS observation and InSAR applied to ALOS-1 radar data. The outputs showed decent agreement between GPS data and InSAR-generated subsidence rate map. In a study in Shanghai, China [50], the X-band sensor Cosmo-SkyMed was used to monitor the subway tunnels and highways by Persistent Scatterer Interferometric Synthetic Aperture Radar (PSInSAR) analysis. In order to detect and monitor ground subsidence caused by tunneling, InSAR time series analysis was applied [59] on RADARSAT-1 and RADARSAT-2 radar data in the urban area of Vancouver, Canada. InSAR technique was also used to monitor landslide displacements induced by excavations related to tunneling in the Northern Apennines, Italy [48]. The tunnel was part of a larger project that contains the improvement of a highway that connects Bologna and Florence. The InSAR outputs showed high agreement with inclinometer and GPS as ground-based monitoring data.

Land surface deformation depends on many factors such as the depth of sediments and the amount of fluid extraction. Therefore, each area may behave differently at different places and different periods. In geotechnical engineering, land subsidence is estimated by considering the following parameters: deformable soil thickness, effective stress variation, and modulus relating the two previous parameters. The changes in the stress state are due to variations in the groundwater level. As the piezometric levels were measured frequently during a period, they are used to determine the groundwater table depth and pore water pressure changes are assumed equal to changes of ground water table [24,60]. Drainage of groundwater in soil deposits can induce huge ground subsidence. Thus, it is imperative to investigate the soil properties of deep geotechnical wells to detect thick compressible sediments particularly in the areas suffering from groundwater extraction.

In this research, we focused on the study area of the Sepulveda Transit Corridor which is planned to improve transportation means between the Los Angeles International Airport and the San Fernando Valley. The previous studies considered the displacements of constructed or under-construction infrastructures such as ground deformations caused by tunnel excavations. The main goal of conducting the present study is to obtain the current ground deformation pattern of a new transit corridor, which can affect its designing criteria and help the designers and decision makers of future constructions. In addition, it is necessary to investigate the subsidence rates in recent years to modify and update the past reports. This paper is organized as follows. First, the study area and the Sepulveda Transit Corridor project is introduced. Second, a brief description of the basic concepts of PSInSAR and the dataset is given. In this study, we used Sentinel-1A SAR images, provided by the European Space Agency (ESA) [61], acquired over the study area from June 2017 to May 2018. Third, the subsidence map derived from PSInSAR analysis is presented. Fourth, piezometric data, GPS observations, and geotechnical properties are provided to assess the outputs. Finally, a framework for evaluation of asymmetric subsidence is proposed. The research objectives of this research are:

- To assess and complement the previous studies on subsidence monitoring in Los Angeles using more recent data.
- To evaluate the PSInSAR results considering soil properties, and hydrological data and GPS information in the area.

- To identify deformation patterns over the study area of the corridor to inform and warn the managers, designers and other stakeholders about the future hazardous consequences.
- To show the variation in displacement rates along the alignment of corridor to help the designers and decision makers of the project to detect the places that require considering immediate solutions to control the current displacements.

2. Study Area: Sepulveda Transit Corridor, Los Angeles, California

The main aim of the Sepulveda Transit Corridor is to enhance transportation between the Los Angeles International Airport (LAX) and the San Fernando Valley. In the current situation, the I-405 highway in this area bears more than 400,000 travel every day and known as one of the most traveled urban freeways in the US [62]. As such, the Los Angeles County Metropolitan Transportation Authority (known as Metro), the agency that controls public transportation for the County of Los Angeles, is conducting a study to assess a range of high-capacity rail transit alternatives between the San Fernando Valley and LAX. The study conducted by Metro is expected to take approximately 20 months, from December 2017 (study kickoff) to Summer/Fall 2019 (study completion). It should be noted that due to the importance of the Sepulveda project, it is funded by the Measure M expenditure plan, with around \$5.7 billion for construction of new transportation service to connect the San Fernando Valley and the Westside, and around \$3.8 billion for extending that transit service between the Westside and LAX [62]. Figure 1 shows the study area of the Sepulveda Transit Corridor covering an area of about 229 km².

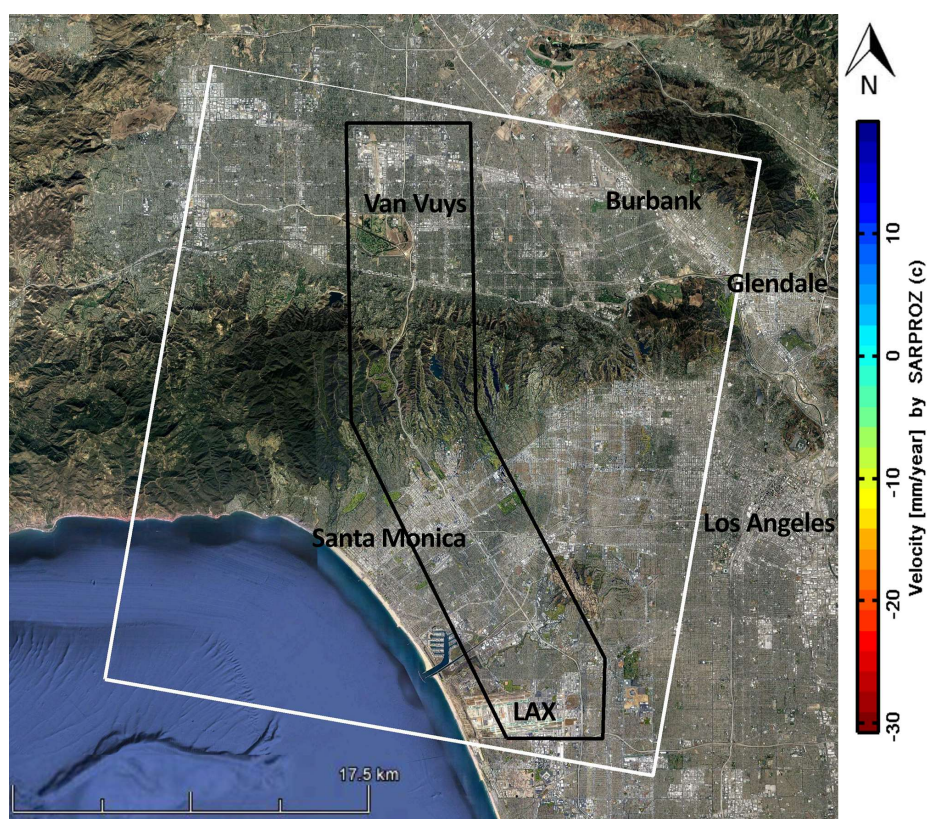


Figure 1. The study area for PSInSAR analysis, including the Sepulveda Transit Corridor.

3. Methodology

3.1. PSInSAR Time Series Analysis

The PSInSAR technique [63] was used in this research to monitor ground deformation through the study area. This technique is one of the powerful SAR time series applications which can analyze

land displacements, particularly in urban areas [64]. PSInSAR looks for Permanent Scatterers [65] with stable scattering properties and also relatively good coherence, over long period intervals in multi-temporal data [66]. For mapping ground deformation, a stack of SAR images of the same area is selected. Afterwards, one single master acquisition is chosen from the stack based on the measured baselines in time and space to achieve an appropriate coherence in interferograms. A reference point is chosen, among the selected Persistent Scatterer Candidates (PSCs), which is relatively unaffected by ground surface displacement. Then, a stack of co-registered Single Look Complex (SLC) images is created using this single master configuration. Phases of each pixel are acquired when the topography and earth curvature influence is removed from the phase. There are a number of factors influenced the acquired phases, such as external DEM inaccuracy, Atmospheric Phase Screen (APS), linear phase ramp, the scatterer movement, and decorrelation and speckle noise. The following equation [67] shows the main factors in the phase calculation.

$$\phi^k = \frac{4\pi}{\lambda} \left(\frac{B_{\perp}^k}{R \sin \theta} \right) h + \frac{4\pi}{\lambda} T^k v + \phi_{atm}^k + \phi_{orb}^k + \phi_{noise}^k \quad (1)$$

where the first term is related to the DEM error (h) because of the external DEM inaccuracy, the second term is related to the linear deformation velocity (v) during the acquisition period. In this equation, ϕ_{atm}^k , ϕ_{orb}^k and ϕ_{noise}^k denote the atmospheric phase delay, the residual orbital error phase, and the temporal and geometrical decorrelation noise, respectively. In this study, we implemented PSInSAR analysis in SARPROZ [4] and the applied processing steps are as the following:

First, each pixel could be a PS candidate if it satisfies the amplitude stability index for the pixel have a value of at least 0.85. The amplitude stability index can be calculated as follow:

$$D_{stab} = 1 - \frac{\sigma_a}{\bar{a}} \quad (2)$$

where D_{stab} , σ_a and \bar{a} are the amplitude stability index, the standard deviation and the mean of amplitude values, respectively. This condition resulted in 57,667 points in the present study.

Second, the unknown parameters of DEM error and the velocity are estimated. For this purpose, the spatial graph of connections between points is considered and the initial parameters are estimated along the connections. Then, the absolute values are achieved by numerical integration considering a reference point as a starting point for the integration. Careful selection of the reference point is a key factor in the accuracy of outputs, as careless reference selection will result in biased parameters for all points.

Finally, a wider set of points are selected considering a spatial coherence of 0.80 and temporal coherence of 0.85 conditions. At this stage, a second approximation of the parameters were applied on the new dataset. Then, all PS points above the temporal coherence threshold were selected for the final estimation. The DEM error, the linear deformation rate along the Line of Sight and the subsidence time series are approximately calculated for the selected PS points.

It should be noted that differentiating between the contributions made to the phase by deformation and atmosphere would be difficult, if we only had two SAR images. As we are using a time-series of SAR images, we can take advantage of this fact that often the atmospheric perturbations exhibit typically high spatial correlation but low temporal correlation [66]. Therefore, we can estimate the atmospheric signal by applying a high-pass filtering in time and a low-pass filtering in space [63]. This is how the atmospheric phase signal was computed and removed from the total phase. Furthermore, the displacement measured by InSAR can be decomposed into two main components: a periodical component and a linear component. The periodical signal is a seasonal deformation phenomenon which is occurred due to the thermal expansion and contraction particularly evident on skyscrapers, bridges, etc. which is not the case in our study area. Therefore, in our work, we only considered the linear trend signal and did not take the seasonality signal into account. Here, we used

descending images which resulted in LOS displacement. So, in order to compare the PSInSAR and GPS data, we used the following equation to obtain GPS measurements in LOS direction [66]:

$$\begin{aligned} GPS_{LOS} = & GPS_{up} \times \cos(\theta_{inc}) \\ & - GPS_{north} \times \cos(\theta_{azi} - 3\pi/2) \times \sin(\theta_{inc}) \\ & - GPS_{east} \times \sin(\theta_{azi} - 3\pi/2) \times \sin(\theta_{inc}) \end{aligned} \quad (3)$$

where GPS_{LOS} is the converted value of GPS data in LOS direction. GPS_{up} , GPS_{north} , and GPS_{east} are the values of GPS observation vector in the up, north, and east directions. θ_{inc} represents incidence angle. The radar images were taken from different incidence angles and the average incident angle is about 43.97° in this study. θ_{azi} represents the heading angle of the satellite from the North (azimuth angle) and is about -9.66° in this study.

3.2. Data Collection

Land deformation measurement by PSInSAR needs sufficient number of SAR images. From literature [67,68], the PS analysis requires at least 20 to 25 SAR images to achieve reliable outputs. Considering this important condition on number of images, we collected 29 descending Sentinel-1A SAR images acquired over the study area during June 2017 and May 2018. After collecting the raw data, we defined the study area with an area of 1019 km^2 to cover the corridor and its neighborhoods. Figure 1 displays the study area. The white line indicates the master area and the black line shows the boundary of the study area of Sepulveda Transit Corridor.

Figure 2 displays the SLC data used in this study and the spatiotemporal baseline configuration of interferometric pairs. To form the interferograms, all images were connected with the master image (5 December 2017). The master image is chosen at the barycenter of the temporal baseline, x-axis, and normal baseline, y-axis, distributions. The dots and lines represent the images and the interferograms, respectively.

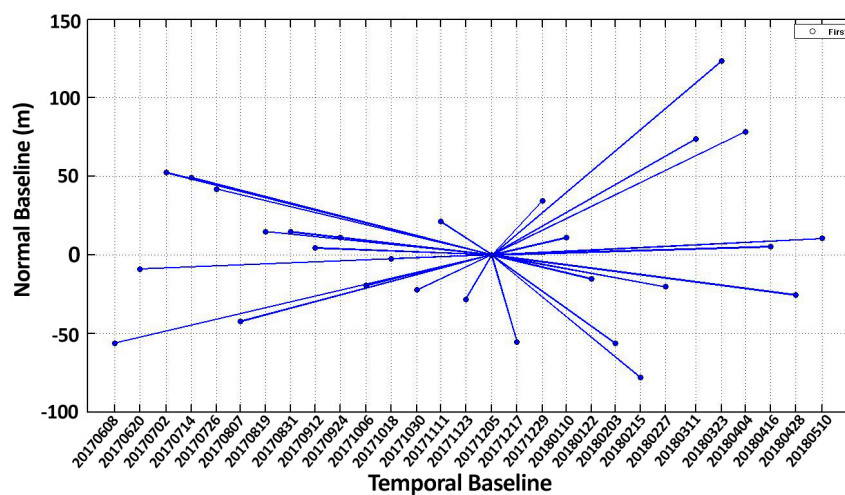


Figure 2. The spatiotemporal baseline configuration of interferometric pairs showing the SLC data in this study (29 images): Sentinel-1A, descending mode (track 71), and polarization VV.

4. Results and Discussion

4.1. Ground Deformation

Applying PSInSAR on a dataset of 29 descending Sentinel-1A radar images resulted in mean velocity map of land deformation in the interest area covering a period between June 2017 and May 2018. It should be noted that based on the spatial coherence of the PSs calculated in the area, most of

the region is covered by a coherence around 0.85 or higher and it can prove the reliability of the monitoring process (Figure 3).

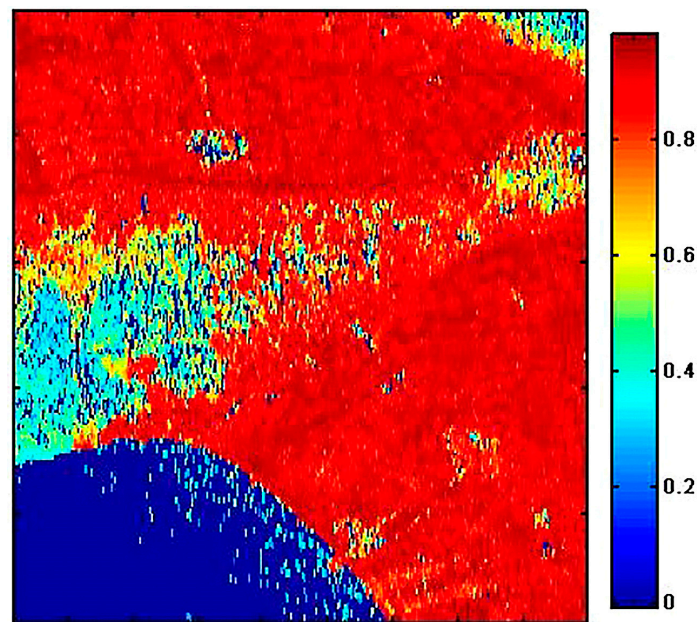


Figure 3. The coherence map obtained in PSInSAR analysis in the study area.

Figure 4 shows the deformation map along the study area of Sepulveda Transit Corridor and its vicinity. In an overall view, we can categorize the corridor into three zones based on the trend of displacement rates: (a) from 0 to 12 km; (b) from 12 to 24 km; and (c) from 24 to 34 km. The red spots in Figure 4 indicates the southeast of the corridor, located over oil extraction sites. In Particular, Figure 5 shows the deformation map in the Inglewood oil field with the maximum subsidence rate about 30 mm/yr. Therefore, it is essential to investigate such engineering solutions as ground stabilization in this site during the study phase and construction phase of Sepulveda corridor. The deformation pattern, also, displays low amounts of uplift (blue features) in south and east of the region meaning that water or gas probably pumped underground to stabilize the subsidence, or it may be as a result of an increase in groundwater level which will be discussed in Section 4.3 of this paper. For instance, the Los Angeles International Airport (LAX) is located in the regions suffering from low amounts of uplift. Green and yellow features through the corridor demonstrate subsidence rates between -15 and 0 mm/yr. Vegetation areas include less coherent PS points; so, there are some regions without sufficient outputs in the extracted maps. It was one of the main reasons to select a large study area to provide more PS points and obtain the deformation trend.

Figure 6 shows the variations in displacement rates (average) along the corridor from south (0 m) to north (34,000 m). In order to estimate the displacement rates in an arbitrary point through the corridor, we proposed a function as Equation (4) derived from the available deformation rates in the location of PS points. Such categorizations can help the designers and decision makers of the project to detect the places, which require solutions to control the probable asymmetric subsidence along the corridor. The asymmetric subsidence is fully explained in Section 4.5.

$$DR \left(\frac{\text{mm}}{\text{year}} \right) = \left\{ \begin{array}{ll} 0.016x + 0.51, & 0 < x < 12 \text{ km} \\ -1.028x + 11.44, & 12 < x < 24 \text{ km} \\ 0.314x - 16.11, & 24 < x < 34 \text{ km} \end{array} \right\} \quad (4)$$

where DR is the displacement rate in each point through the alignment of Sepulveda Transit Corridor, and x (km) is the distance from the start point (LAX).

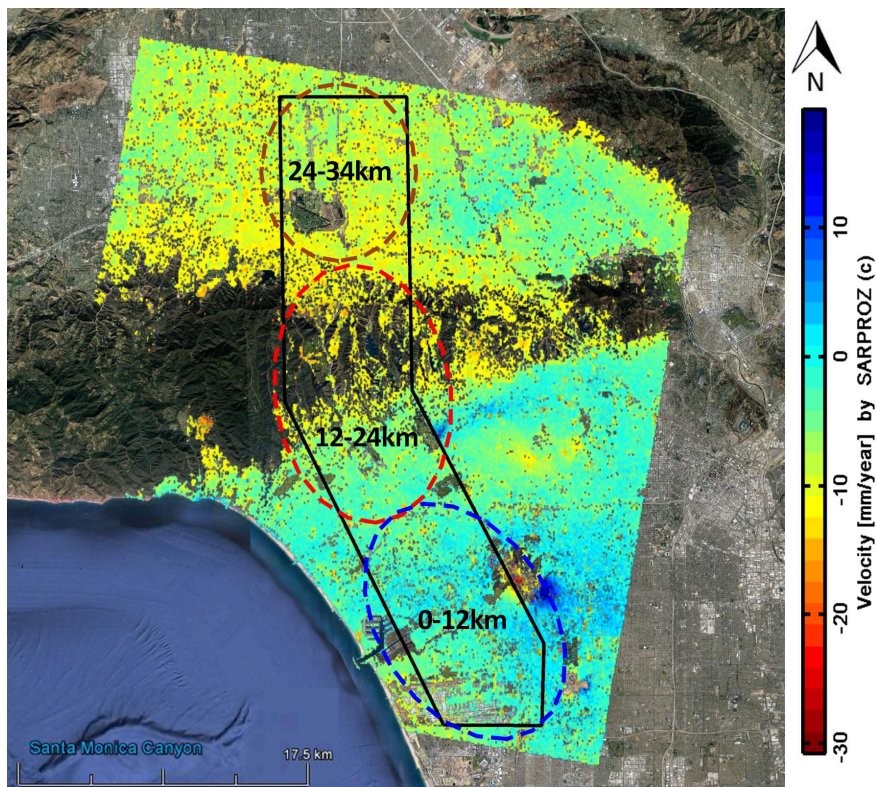


Figure 4. Mean velocity map of land deformation (mm/yr) in the region covering a period between June 2017 and May 2018 overlapped onto Google Earth high-resolution imagery. The black line shows the boundary of Sepulveda Transit Corridor study area. The corridor categorized into three zones based on the trend of displacement rates: (a) from 0 to 12 km; (b) from 12 to 24 km; and (c) from 24 to 34 km.

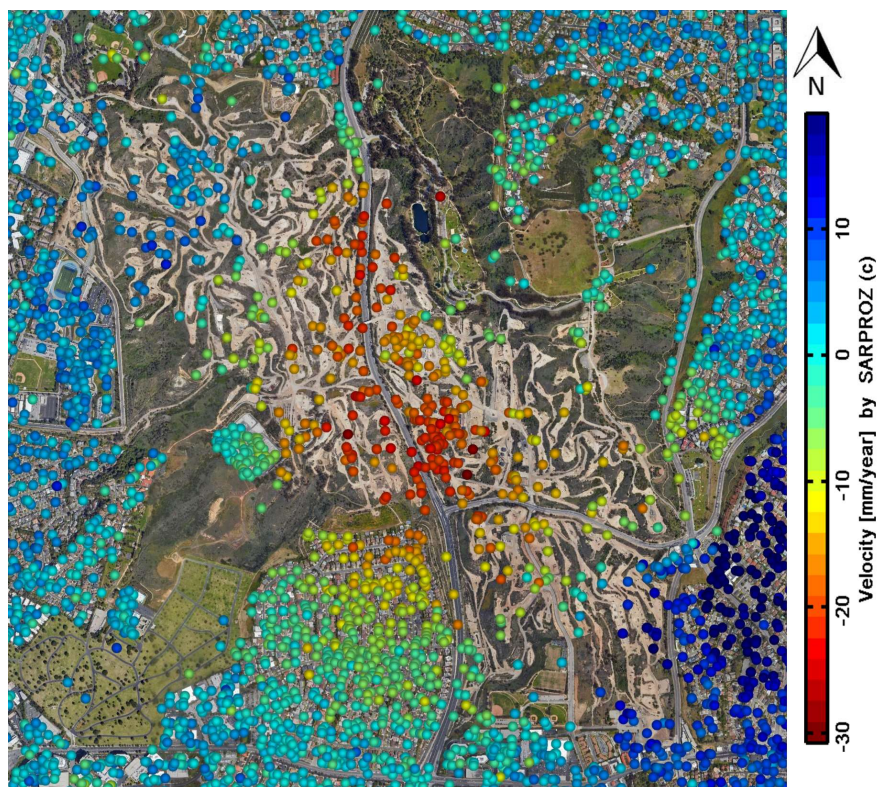


Figure 5. Deformation map in the Inglewood area.

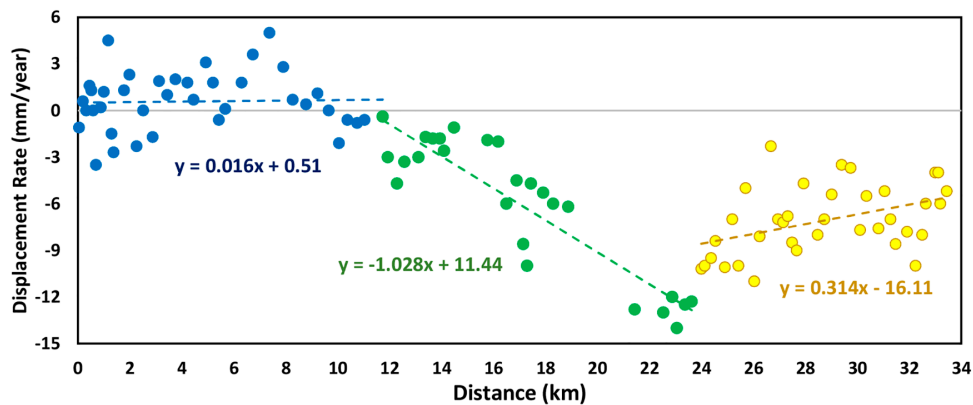


Figure 6. Average rate of displacement along the Sepulveda Transit Corridor from south to north.

4.2. GPS Monitoring

In order to assess the results of PSInSAR analysis, the GPS observations and piezometric data are collected in the present study. Figure 7 shows the location of GPS stations and piezometric wells (P1 to P6). The characteristics and information of the well points are fully explained in Section 4.3.

GPS data has high temporal resolution because of continuous measurements while the PSInSAR method provides high spatial resolution and lower temporal resolution compared to data from GPS stations. Thus, the integration of GPS and PSInSAR measurements can be used to interpret the land displacements. In order to evaluate the PSInSAR results in the previous section, GPS data [69] were collected and introduced in Table 1. Eight stations are represented which two of them (DSHS and FXHS) are inactive since 2011. So, we considered six active stations to compare their results with the PSInSAR outputs in their locations and then, two stations (BRAN and NOPK) with more noises and insufficient observations were removed. Figure 8 shows the comparison between PSInSAR-derived time series deformation and the corresponding GPS observations. For this comparison, the RMSE was computed between each PSInSAR output and GPS measurement and demonstrated relatively good agreement between them. Lacking sufficient number of GPS stations is a significant weakness of GPS stations in monitoring the land displacements compared to SAR Interferometry. Also, the fluctuations in GPS results referred to seasonal effects and the instrument inherit errors [69]. These are the main disadvantageous or weaknesses of GPS observations compared to the SAR analysis performed in the present study.

Table 1. GPS Stations in the Study Area.

GPS Station	Start Date	Location		Current Situation
		Long.	Lat.	
DSHS	1999	−118.3485°	34.0239°	Inactive (since 2011)
FXHS	1999	−118.3595°	34.0806°	Inactive (since 2011)
BRAN	1994	−118.2771°	34.1849°	Active
NOPK	1999	−118.3480°	33.9797°	Active
LAPC	1999	−118.5747°	34.1819°	Active
LFRS	1999	−118.4128°	34.0951°	Active
CSN1	1999	−118.5238°	34.2536°	Active
WRHS	1999	−118.4276°	33.9582°	Active

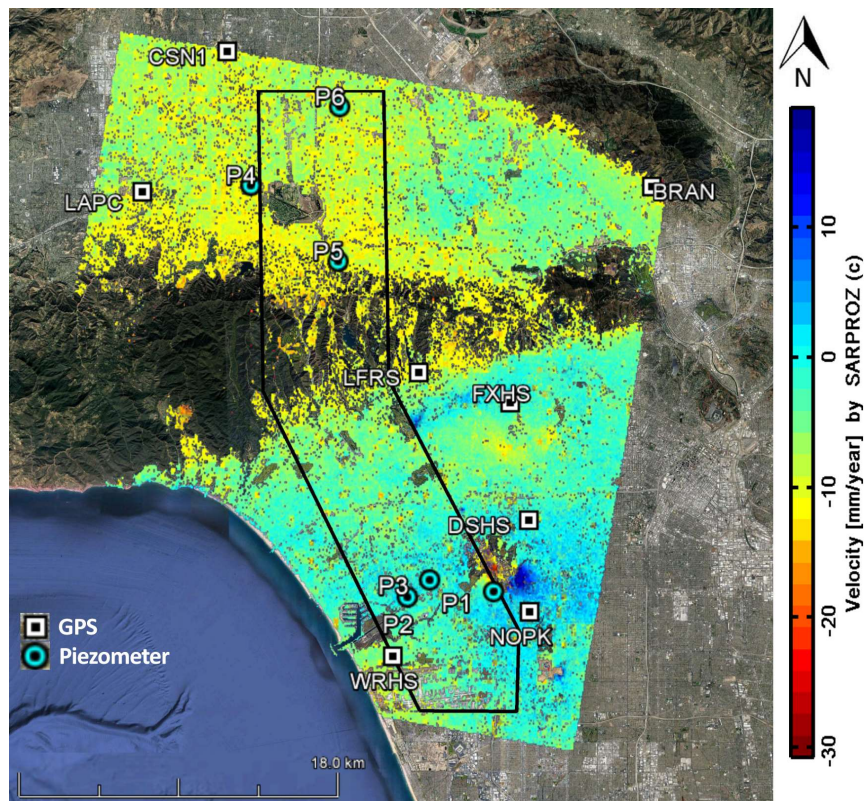


Figure 7. The location of GPS stations (squares) and piezometers (circles) in the study area.

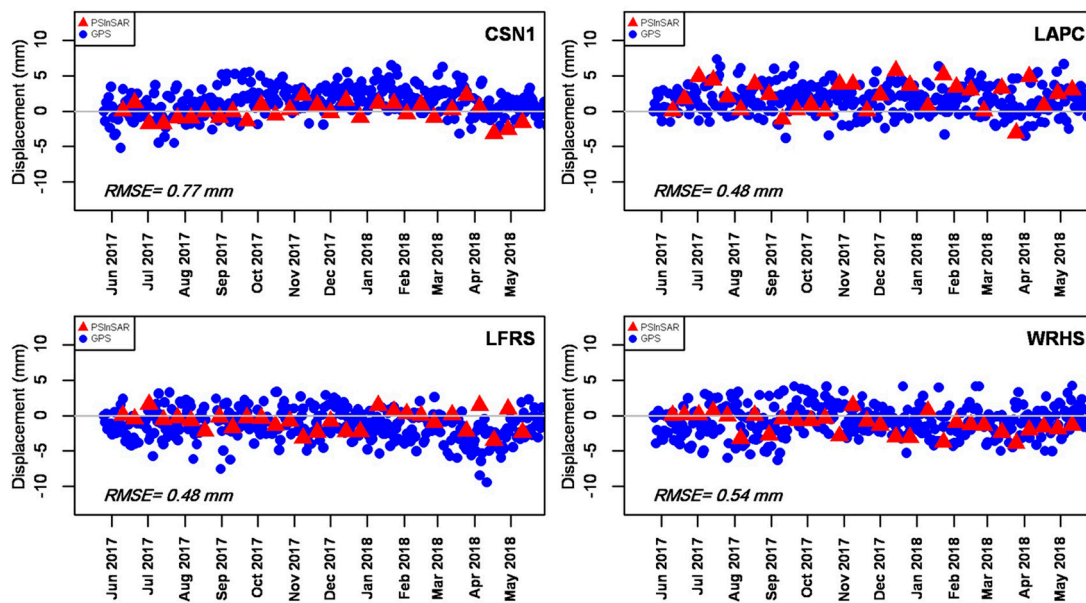


Figure 8. Comparison between PSInSAR-derived time series deformation (red triangles) and GPS observations (blue dots), Line-of-Sight direction, from June 2017 to May 2018.

Table 2 shows the comparison between GPS and PSInSAR deformation rates in long-term and short period. Overall, from Table 2 it can be found that the Standard Deviation of GPS data is in average (2.04) bigger than the Standard Deviation of PSInSAR data (1.56) which is because there are more noises in GPS measurements.

Table 2. The comparison between GPS and PSInSAR outputs.

GPS Station	GPS Observation		PSInSAR Deformation Rate from 2017 to 2018 (mm/yr)	Standard Deviation of GPS Data (mm)	Standard Deviation of PSInSAR Data (mm)	RMSE (mm)
	Long-Term Deformation Rate from 1995 to 2018 (mm/yr)	Deformation Rate from 2017 to 2018 (mm/yr)				
WRHS	+0.73	−2.61	−2.23	2.16	1.41	0.54
LAPC	+0.84	+0.49	+0.31	1.94	2.13	0.48
LFRS	−0.19	−0.72	−0.49	2.09	1.37	0.48
CSN1	+0.20	+0.08	+0.06	1.95	1.34	0.77

4.3. Monitoring of Groundwater Level Variations

According to the literature, one of the main reasons for ground displacements in the study area is water withdrawal or increase in groundwater level, except the red spots in the deformation map which suffer from oil extraction in the region. Based on the project's official report [70], groundwater is highly variable along the extent of the project corridor. Unfortunately, the groundwater depths and elevations are not well-documented throughout the Santa Monica Mountains. The historical groundwater level data of the Inglewood quadrangle [71] shows the groundwater depths for the southern end of the Sepulveda corridor and indicates that groundwater level in the southerly part of the project alignment is about 12 m below grade and deepens to 15 m as the corridor extends northward through Inglewood city. In addition, data from another project in the region, called the Crenshaw /LAX Transit Corridor Project, show the areas along the southern part of the project corridor have measured depths of groundwater ranging between 12 and 27.5 m below grade. As the corridor bends northwest, the groundwater moves closer to the ground surface, with an approximate depth of 3 m or less [70].

Much of the I-405 highway in Sepulveda Canyon along the Santa Monica Mountains is not known to encounter shallow groundwater [72]. Based to groundwater monitoring data of the widening project of I-405 corridor from 2008 to 2009, groundwater was reached at depths greater than 21 m below the corridor surface. However, higher groundwater levels were observed during drilling between 1958 and 2007 for the purpose of as-built data at bridge locations through the existing Sepulveda Pass. This data contains groundwater depths between 0.6 and 24 m below existing grade [70]. The historical groundwater level data of the Van Nuys quadrangles [72] and the San Fernando [73] displays groundwater to be progressively shallower northward from the base of the Santa Monica Mountains where the groundwater depth is 12 m below grade and rises to 0 m below grade where the transit corridor intersects the 101 freeway. From the 101 freeway north along the corridor, the groundwater ascends progressively northward along alignment up to approximately 67 m below grade, where it reaches an abrupt groundwater barrier at the location of the Mission Hills fault. At this area, where the I-405 meets SR-118, the groundwater jumps to 12 m below grade. This site is where the San Fernando fault exists and groundwater data is probably not sufficient enough to show accurate contours due to the extensive faulting and deformation within the area [70].

We monitored the variations in groundwater level in the study area of Sepulveda Transit Corridor. Figure 9 shows temporal evaluation of groundwater level changes for the piezometers (the locations of piezometers are shown in Figure 7). Table 3 shows the overall trend of groundwater level changes at the studied piezometric wells and their corresponding PSInSAR deformation rate. The groundwater level in the location of P5 experienced several fluctuations and dramatically decreased since 2008. Surprisingly, this point shows the maximum subsidence rate among the piezometers with 11 mm/yr. On the other hand, the water level remained stable during the period at P1 and P2. Both piezometers have negligible displacements at their locations based on PSInSAR outputs. The rising trend of groundwater in piezometer P3 confirms the PSInSAR analysis which shows uplift of almost 3 mm/yr in P3 location. It should be noted that PSInSAR computes the total displacement rate and there may be some other factors as parts of ground movements. In order to investigate the relation between land

deformation rate and water level variation it is imperative to know soil properties that are thoroughly explained in Section 4.4.

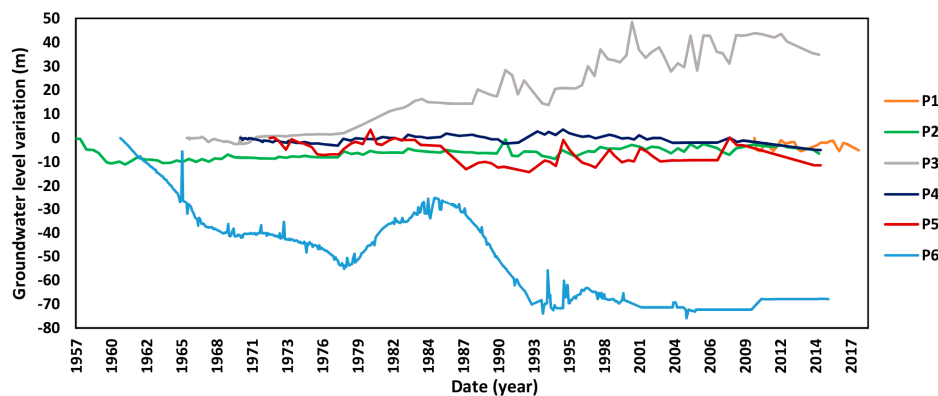


Figure 9. Temporal evaluation of groundwater level variations for six piezometers (P1 to P6) located in the study area of Sepulveda Transit Corridor.

Table 3. Overall characteristics of the studied piezometric wells.

Piezometric Well	Deformation Rate by PSInSAR (mm/yr)	Δh (m)	Δt (year)	$\Delta h/\Delta t$ (mm/yr)	Overall Trend of Ground Water Level Variations
P1	0	5.08	8	0.64	Remained stable.
P2	0	6.5	59	0.11	Remained stable.
P3	+3	−34.9	49	−0.71	Increased during the whole period and slightly decreased after 2009.
P4	−6.7	5	45	0.11	Relatively stable up to 1995 and then decreased slightly up to now.
P5	−11	11.4	43	0.27	Experienced several fluctuations, but decreased after 2008 up to now.
P6	−5	67.9	55	1.23	Decreased about 40 m between 1985 and 1995 and relatively stable up to now.

4.4. Geological Characteristics of the Sepulveda Project and Hydrogeology of Basins

The Los Angeles area consists of several basins containing groundwater systems. The Sepulveda project extends through numerous geologic characteristics of Los Angeles County within the Santa Monica (SM) and San Fernando (SF) Groundwater Basins. Table 4 shows the overall properties of SM and SF basins. The recharge of SF is by natural streamflow from the surrounding mountains, precipitation falling on impervious areas, reclaimed wastewater, and industrial discharges [74]. The replenishment of SM is mainly by percolation of precipitation and surface runoff onto the sub-basin from the SM Mountains [75].

The SF Valley Basin is bounded by the Santa Susana Mountains on the north and northwest, the San Gabriel Mountains on the north and northeast, the San Rafael Hills on the east, the Santa Monica Mountains and Chalk Hills on the south, and the Simi Hills on the west. The groundwater in this basin is mainly unconfined with some confinement. Also, several structures disturb the flow of groundwater through this basin such as faults and subsurface dams [74]. The groundwater in the SM Basin is mainly confined and this basin underlies the northwestern part of the Coastal Plain of Los Angeles Basin. SM bounded by impermeable rocks of the SM Mountains on the north and by the Ballona escarpment on the south [75].

The main water-producing units of SM include the relatively coarse-grained sediments of the Recent Alluvium, Lakewood Formation, and San Pedro Formation [76]. The Recent Alluvium reaches a maximum thickness of around 27 m and comprises the clays of the Bellflower aquiclude and the underlying Ballona aquifer, depositing gravels resulting in the present Ballona Gap structure. These gravels are dominant at an approximate depth of 15 m. The Ballona aquifer is generally separated from the underlying San Pedro Formation by the confining layer [77]. The Lakewood Formation seems to be present only in the northern half of the SM Basin. The most significant water-bearing units

are the sands and gravels within the San Pedro Formation. The Silverado aquifer of the San Pedro Formation has the greatest lateral extent and saturated thickness, and is considered as the main source of groundwater. The average thickness of San Pedro Formation is about 60 m in the SM Basin. Beneath the Silverado aquifer are relatively low-permeability sediments of the lower San Pedro and upper Pico formations [77].

The Sepulveda project cuts through San Fernando Valley in the north and extends through the Santa Monica Mountains in the south. The corridor is underlain by a layer of horizontal Quaternary sediment and also Tertiary-age sediments and sedimentary rocks which faced deformation into folds and offset by faults. Sedimentary and metamorphic bedrock are exposed with colluvial and alluvial soil at the surface at high elevations such as Santa Monica Mountains. In the north and south of Santa Monica Mountains, there is a thick layer of alluvial sediments. Also, the portion of the corridor located above San Fernando Valley is underlain by up to 600 m of alluvial deposits and a layer of Cretaceous-aged crystalline bedrock which exists below the alluvium [78]. The southern part of the project corridor, located in the Los Angeles Basin, is underlain by unconsolidated Quaternary-aged sandy deposits. These deposits can be subdivided into a loose unconsolidated Holocene-age layer and late-Pleistocene sediments. Also, hard rocks only exist in the mountainous portion of the basin at depth of 1500 m to 9000 m.

Figure 10 shows surface soil map of the study area including various soil types (the map is created based on raw soil data provided by the Los Angeles County Department of Public Works). In order to investigate the subsidence and uplift in the region, it is needed to study the soil properties in depth. Figure 11 displays the location of nine geotechnical boreholes in the region. The raw data of boreholes are collected from geotechnical report of the corridor and a number of geotechnical reports in the area [79–84].

Groundwater pumping has the potential to cause subsidence which can induce structural impacts. Induced subsidence is caused by the lowering of groundwater levels causing compaction of the aquifer materials to a point that the ground surface changes elevation. As water is withdrawn and groundwater levels declines, the effective pressure in the drained sediments increases. Compressible layers then compact under the over-pressure burden that is no longer compensated by hydrostatic pressure. The subsequent subsidence, includes both a component of elastic (recoverable) and inelastic (unrecoverable) subsidence, and is most pronounced in poorly compacted sediments. As a historical subsidence example, there is evidence for subsidence near Redondo Beach, in south of SM, that is attributed to oil and gas extraction [85]. From literature, a review of the geotechnical logs for wells completed in the SM Basin does not show considerable evidence of a thick compressible layer. Groundwater levels have also experienced significant drawdown in the past prior to the importation of water into the area. So, inelastic subsidence, which is of most concern, by nature can only occur once; consequently, any potential subsidence would have already occurred. Land subsidence in the study area does not appear to be a significant concern [76]. It should be added that as shown in Figure 12, investigation of the boreholes indicates some layers of fine-grained materials in some parts of the study area, which are susceptible to variations in groundwater level, an indication of the necessity of more detailed geotechnical investigations for the future constructions in the region.

Table 4. Overall characteristics of San Fernando (SF) and Santa Monica (SM) basins [74,75].

Basin	Confined/Unconfined	Recharge	Groundwater Level Trend
SF	Mainly unconfined with some confinement	Natural streamflow from the surrounding mountains, precipitation falling on impervious areas, reclaimed wastewater, and industrial discharges.	fairly stable over about the past 20 years
SM	Confined	Mainly by percolation of precipitation and surface runoff onto the sub-basin from the SM Mountains.	fairly stable over about the past 20 years

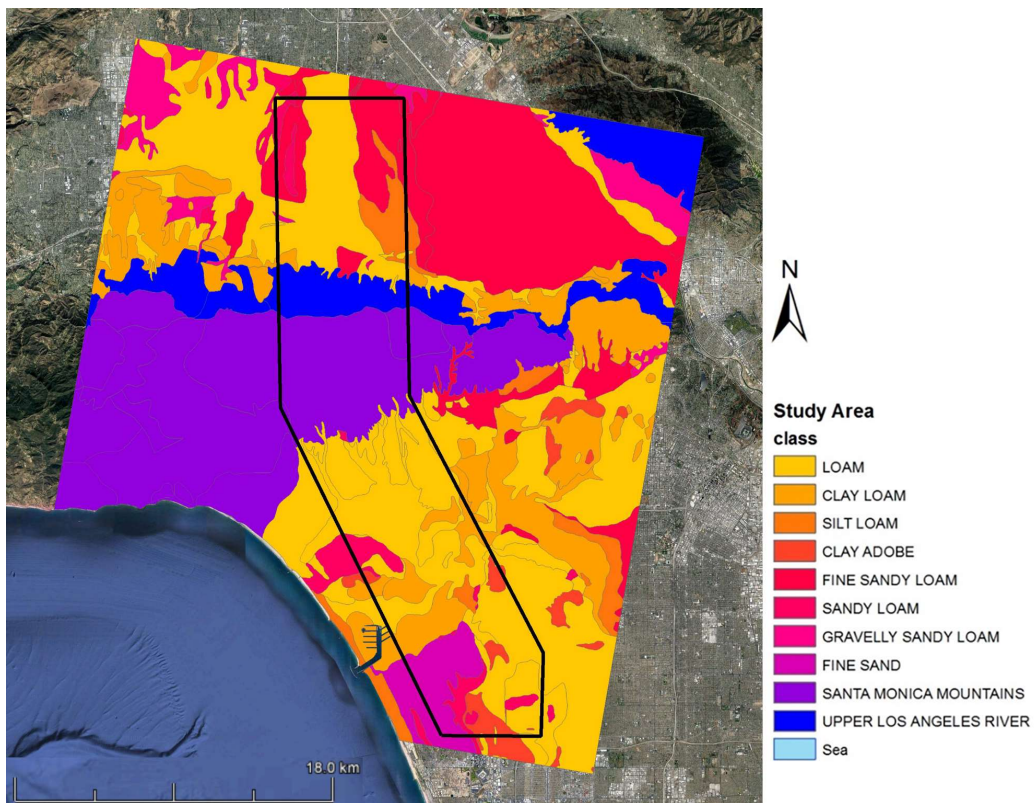


Figure 10. Surface soil map of the study area. The map is created based on raw soil data provided by the Los Angeles County Department of Public Works, Water Resources Division.

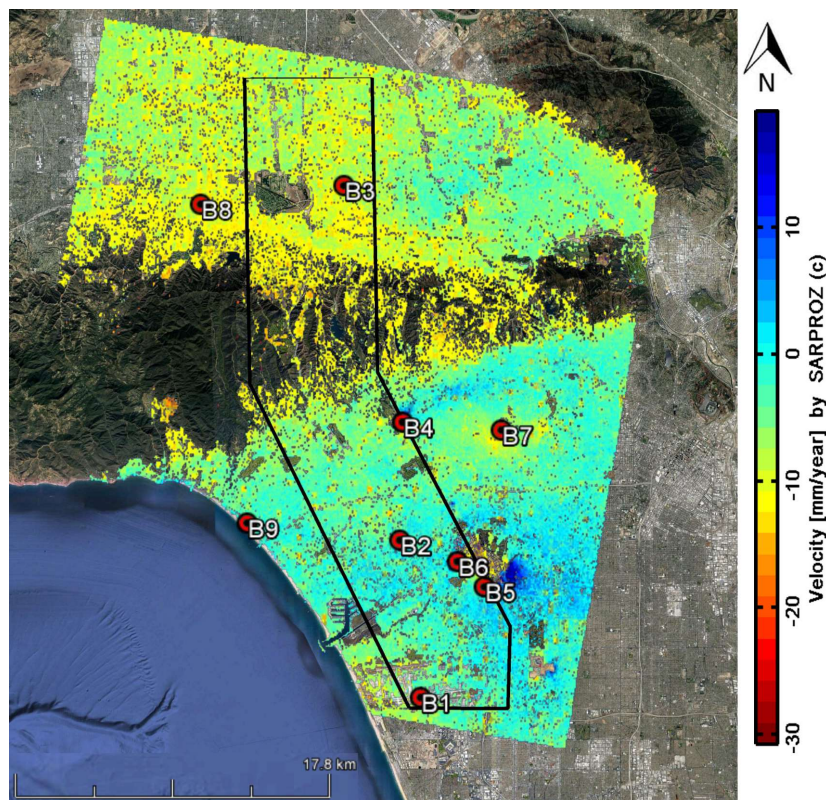


Figure 11. The location of Lithological logs.

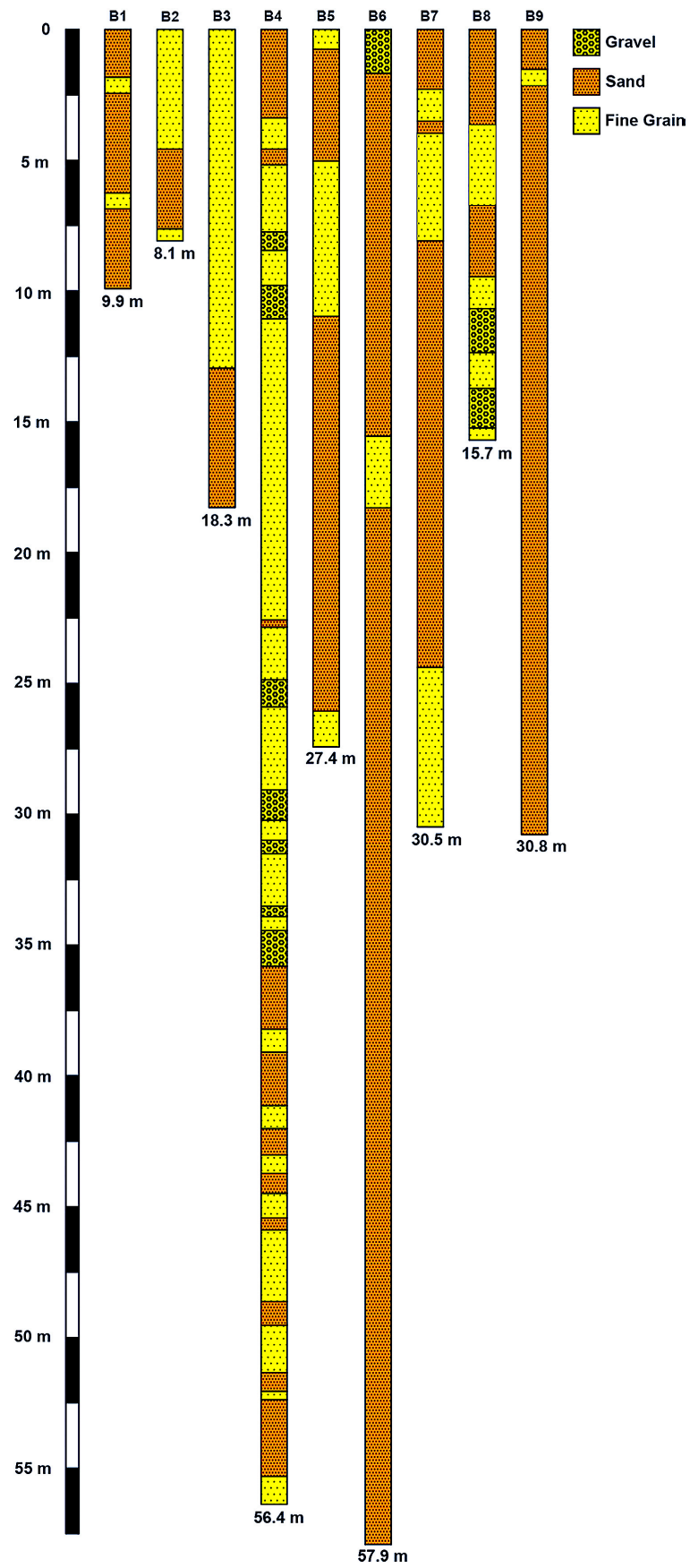


Figure 12. Lithological logs in the interest area.

4.5. Asymmetrical Subsidence

In most cases, the subsidence profile during the design phase of construction is considered symmetrical due to the assumptions inherent in the analysis and oversimplifications of the ground behavior. However, the ground behavior is not simple but instead very complex with different types of materials and different stress-strain responses. Such complexities can lead to the ground surface displacement to occur in such a way that it is not symmetrical (asymmetrical). In other words, asymmetrical subsidence means the difference in the amount of ground deformation between two near points which could be devastating especially to the available infrastructure and the infrastructure under construction such as the Sepulveda Transit Corridor. Asymmetry in subsidence can be observed in such industries [86–88] as mining, tunneling, groundwater withdrawal, oil and gas extraction, and geothermal fluid withdrawal.

Asymmetrical ground subsidence can be economically devastating to structures at surface. The heterogeneity of the ground layers (soil or rock) contribute to difficult estimation of asymmetrical subsidence [86,89]. As discussed in the Section 4.4, the Sepulveda project extends through numerous geologic characteristics and the region suffers from ground deformations. Accordingly, it is necessary to provide a certain procedure for the evaluation of asymmetric subsidence. Therefore, to detect the areas suffering from asymmetric subsidence, we propose a simplified version of strain rate based on the PSInSAR outputs to calculate Asymmetric Subsidence Index (*ASI*) as the following steps:

In step 1, consider two close PS points through the corridor length (L_L) and two PS points on/near both sides of the corridor width (L_W).

In step 2, determine the displacement rate (*DR*) of the selected points in step 1 based on PSInSAR analysis.

In step 3, calculate the *ASI* along length (ASI_L) by the ratio between the displacement rates (step 2) and length (L_L), Equation (5). Calculate the *ASI* along width (ASI_W) by the ratio between the displacement rates and length (L_W), Equation (6).

$$ASI_L = \frac{d_L}{L_L} = \left| \frac{DR_2 - DR_1}{L_L} \right| \quad (5)$$

where DR_1 and DR_2 are the displacement rate of the PS points in length. For instance, the value of DR_1 and DR_2 of the Sepulveda Transit Corridor can be estimated by Equation (4).

$$ASI_W = \frac{d_W}{L_W} = \left| \frac{DR_{Right} - DR_{Left}}{L_W} \right| \quad (6)$$

where DR_{Right} and DR_{Left} are the displacement rate of the PS points in width.

In step 4, the final Asymmetric Subsidence Index of the interest area is defined as the maximum of ASI_L and ASI_W , Equation (7).

$$ASI = \max\{ASI_L, ASI_W\} \quad (7)$$

It should be noted that for practical purposes, it is more accurate and better to use vertical displacements, to provide much more meaningful result, instead of line-of-sight deformations in engineering problems. The higher the value of *ASI*, the higher the asymmetry of the deformation and the value of allowable *ASI* depends on the sensitivity of each especial structure. Therefore, we suggest computing *ASI* for new constructions for considering possible evaluations and solutions. For practical calculation, we suggest considering the average of *ASI* values for a several points. Clearly, the amount of d_L and d_W must be less than allowable displacement which depends on the sensitivity of each particular project. Figure 13 displays a simple example in the study area to show how to calculate the *ASI*. The required calculations for this example are shown in Table 5 and the computed *ASI* in this example is negligible; so, it can be assumed symmetrical. The proposed framework can be easily used in engineering applications compared to the more common strain rate analysis.



Figure 13. An example for ASI calculation for an infrastructure in the study area.

Table 5. The ASI calculation for the example.

Point	Temporal Coherence	DR (mm/yr)	Length (m)	ASI	Max ASI
A	0.99	-14.6	$L_{AB} = 53.4$	$ASI_L = \left \frac{-14.6 - (-14.1)}{53.4 \times 1000} \right = 9 \times 10^{-6}$	3×10^{-5}
B	0.99	-14.1			
C	0.99	-13.1	$L_{CD} = 31.2$	$ASI_W = \left \frac{-13.1 - (-14.1)}{31.2 \times 1000} \right = 3 \times 10^{-5}$	
D	0.99	-14.1			

5. Conclusions

The main aim of this research was to obtain the land displacements along a new metro tunnel under preliminary study in Los Angeles, CA called Sepulveda Transit Corridor; to detect the most crucial areas suffering from subsidence or uplift; and to complement the previous reports in Los Angeles. For this purpose, we applied Persistent Scatterer Interferometric Synthetic Aperture Radar using 29 Sentinel-1A radar images from 2017 to 2018. The outputs demonstrated a high-rate of subsidence in the Inglewood field that is near the south portion of the Sepulveda Transit Corridor. Finally, we used the PSInSAR outputs to calculate Asymmetric Subsidence Index (ASI). The main conclusions of the present study can be drawn as the following:

- The results of this paper showed that the ground subsidence in northern portion of the Sepulveda Transit Corridor is continuous with subsidence rates between 1 and 14 mm/yr and a high-rate of subsidence (30 mm/yr) occurs in the Inglewood field near the south portion of the corridor, which may cause irreversible consequences in the future.

- Based on the variation in displacement rates along the corridor, we categorized the corridor into three zones to help the designers and decision makers of the project to detect the places which require considering solutions to control the probable asymmetric subsidence along the corridor.
- The ground water extraction rate and geotechnical properties in the area both strongly influence the rate and the distribution of subsidence.
- Collecting deep geotechnical boreholes indicated fine-grained layers in the region. This observation confirmed the necessity of more detailed geotechnical investigations in the interest area.
- There are not a sufficient number of piezometers to detect the groundwater level and accurate in-situ instruments such as GPS stations and extensometers to monitor the land displacements in this area. Therefore, for future researches, we recommend adding more piezometers and instruments particularly in the places suffering from continuous subsidence or uplift.
- Asymmetrical subsidence can be devastating to structures. Because of the heterogeneity of the ground layers, it is difficult to estimate asymmetrical subsidence. So, a simplified framework was proposed based on PSInSAR outputs to evaluate asymmetric subsidence.

Author Contributions: Conceptualization, M.K.; Data curation, M.K. and B.A.; Formal analysis, M.K. and B.A.; Investigation, M.K., B.A., E.G.T., M.S. and P.R.; Methodology, M.K., B.A., Y.M., P.R., E.G.T. and M.S.; Software, M.K. and B.A.; Supervision, Y.M.; Validation, M.K., B.A., E.G.T., P.R. and M.S.; Writing—original draft, M.K. and B.A.; Writing—review & editing, M.K., B.A., Y.M., P.R., E.G.T., and M.S.

Funding: This research received no external funding.

Acknowledgments: Authors are sincerely grateful to the European Space Agency (ESA) for providing Sentinel-1A data. We convey our gratitude to the United States Geological Survey (USGS) for GPS data, Los Angeles County Department of Public Works (LACDPW) for providing groundwater data, the Los Angeles County Metropolitan Transportation Authority for the required data of Sepulveda Pass Corridor, Daniele Perissin for providing SARPROZ, Aron Meltzner and Fatemeh Foroughnia for helpful discussions.

Conflicts of Interest: The authors declare no conflict of interest.

References

1. Bull, W.B.; Poland, J.F. *Land Subsidence Due to Ground-Water Withdrawal in the Los Banos-Kettleman City Area, California: Part 3. Interrelations of Water-Level Change, Change in Aquifer-System Thickness, and Subsidence*; US Government Printing Office: Washington, DC, USA, 1975; Volume 3.
2. Galloway, D.L.; Hudnut, K.W.; Ingebritsen, S.; Phillips, S.P.; Peltzer, G.; Rogez, F.; Rosen, P. Detection of aquifer system compaction and land subsidence using interferometric synthetic aperture radar, Antelope Valley, Mojave Desert, California. *Water Resour. Res.* **1998**, *34*, 2573–2585. [[CrossRef](#)]
3. Poland, J.; Davis, G. Subsidence of the land surface in the Tulare—Wasco (Delano) and Los Banos—Kettleman City area, San Joaquin Valley, California. *EOS Trans. Am. Geophys. Union* **1956**, *37*, 287–296. [[CrossRef](#)]
4. Perissin, D.; Wang, Z.; Wang, T. The SARPROZ InSAR tool for urban subsidence/manmade structure stability monitoring in China. In Proceedings of the 34th International Symposium on Remote Sensing of Environment, Sydney, Australia, 10–15 April 2011.
5. Osmanoglu, B.; Dixon, T.H.; Wdowinski, S.; Cabral-Cano, E.; Jiang, Y. Mexico City subsidence observed with persistent scatterer InSAR. *Int. J. Appl. Earth Obs.* **2011**, *13*, 1–12. [[CrossRef](#)]
6. López-Quiroz, P.; Doin, M.-P.; Tupin, F.; Briole, P.; Nicolas, J.-M. Time series analysis of Mexico City subsidence constrained by radar interferometry. *J. Appl. Geophys.* **2009**, *69*, 1–15. [[CrossRef](#)]
7. Chai, J.C.; Shen, S.L.; Zhu, H.H.; Zhang, X.L. Land subsidence due to groundwater drawdown in Shanghai. *Geotechnique* **2004**, *54*, 143–147. [[CrossRef](#)]
8. Shen, S.L.; Xu, Y.S. Numerical evaluation of land subsidence induced by groundwater pumping in Shanghai. *Can. Geotech. J.* **2011**, *48*, 1378–1392. [[CrossRef](#)]
9. Shen, S.L.; Ma, L.; Xu, Y.S.; Yin, Z.Y. Interpretation of increased deformation rate in aquifer IV due to groundwater pumping in Shanghai. *Can. Geotech. J.* **2013**, *50*, 1129–1142. [[CrossRef](#)]
10. Maghsoudi, Y.; van der Meer, F.; Hecker, C.; Perissin, D.; Saepuloh, A. Using PS-InSAR to detect surface deformation in geothermal areas of West Java in Indonesia. *Int. J. Appl. Earth Obs.* **2017**. [[CrossRef](#)]

11. Abidin, H.Z.; Andreas, H.; Gumilar, I.; Fukuda, Y.; Pohan, Y.E.; Deguchi, T. Land subsidence of Jakarta (Indonesia) and its relation with urban development. *Nat. Hazards* **2011**, *59*, 1753. [[CrossRef](#)]
12. Chaussard, E.; Amelung, F.; Abidin, H.; Hong, S.-H. Sinking cities in Indonesia: ALOS PALSAR detects rapid subsidence due to groundwater and gas extraction. *Remote Sens. Environ.* **2013**, *128*, 150–161. [[CrossRef](#)]
13. Marfai, M.A.; King, L. Monitoring land subsidence in Semarang, Indonesia. *Environ. Geol.* **2007**, *53*, 651–659. [[CrossRef](#)]
14. Teatini, P.; Ferronato, M.; Gambolati, G.; Bertoni, W.; Gonella, M. A century of land subsidence in Ravenna, Italy. *Environ. Geol.* **2005**, *47*, 831–846. [[CrossRef](#)]
15. Stramondo, S.; Saroli, M.; Tolomei, C.; Moro, M.; Doumaz, F.; Pesci, A.; Loddo, F.; Baldi, P.; Boschi, E. Surface movements in Bologna (Po plain—Italy) detected by multitemporal DInSAR. *Remote Sens. Environ.* **2007**, *110*, 304–316. [[CrossRef](#)]
16. Raucoules, D.; Le Mouélic, S.; Carnec, C.; Maisons, C.; King, C. Urban subsidence in the city of Prato (Italy) monitored by satellite radar interferometry. *Int. J. Remote Sens.* **2003**, *24*, 891–897. [[CrossRef](#)]
17. Rosi, A.; Tofani, V.; Agostini, A.; Tanteri, L.; Stefanelli, C.T.; Catani, F.; Casagli, N. Subsidence mapping at regional scale using persistent scatterers interferometry (PSI): The case of Tuscany region (Italy). *Int. J. Appl. Earth Obs.* **2016**, *52*, 328–337. [[CrossRef](#)]
18. Del Soldato, M.; Farolfi, G.; Rosi, A.; Raspini, F.; Casagli, N. Subsidence evolution of the Firenze–Prato–Pistoia plain (Central Italy) combining PSI and GNSS data. *Remote Sens.* **2018**, *10*, 1146. [[CrossRef](#)]
19. Motagh, M.; Djamour, Y.; Walter, T.R.; Wetzel, H.U.; Zschau, J.; Arabi, S. Land subsidence in Mashhad Valley, northeast Iran: results from InSAR, levelling and GPS. *Geophys. J. Int.* **2007**, *168*, 518–526. [[CrossRef](#)]
20. Akbari, V.; Motagh, M. Improved ground subsidence monitoring using small baseline SAR interferograms and a weighted least squares inversion algorithm. *IEEE Geosci. Remote Sens.* **2012**, *9*, 437–441. [[CrossRef](#)]
21. Dehghani, M.; Valadan Zoej, M.J.; Entezam, I.; Mansourian, A.; Saatchi, S. InSAR monitoring of progressive land subsidence in Neyshabour, northeast Iran. *Geophys. J. Int.* **2009**, *178*, 47–56. [[CrossRef](#)]
22. Motagh, M.; Shamshiri, R.; Haghghi, M.H.; Wetzel, H.-U.; Akbari, B.; Nahavandchi, H.; Roessner, S.; Arabi, S. Quantifying groundwater exploitation induced subsidence in the Rafsanjan plain, southeastern Iran, using InSAR time-series and in situ measurements. *Eng. Geol.* **2017**, *218*, 134–151. [[CrossRef](#)]
23. Sadeghi, Z.; Zoej, M.J.V.; Dehghani, M.; Chang, N.B. Enhanced algorithm based on persistent scatterer interferometry for the estimation of high-rate land subsidence. *J. Appl. Remote Sens.* **2012**, *6*. [[CrossRef](#)]
24. Khorrami, M.; Abrishami, S.; Maghsoudi, Y. Mashhad Subsidence Monitoring by Interferometric Synthetic Aperture Radar Technique. *AUT J. Civ. Eng.* **2018**. [[CrossRef](#)]
25. Foroughnia, F.; Nemati, S.; Maghsoudi, Y.; Perissin, D. An iterative PS-InSAR method for the analysis of large spatio-temporal baseline data stacks for land subsidence estimation. *Int. J. Appl. Earth Obs.* **2019**, *74*, 248–258. [[CrossRef](#)]
26. Hu, J.; Ding, X.L.; Li, Z.W.; Zhang, L.; Zhu, J.J.; Sun, Q.; Gao, G.J. Vertical and horizontal displacements of Los Angeles from InSAR and GPS time series analysis: Resolving tectonic and anthropogenic motions. *J. Geodyn.* **2016**, *99*, 27–38. [[CrossRef](#)]
27. Perissin, D. Interferometric SAR Multitemporal Processing: Techniques and Applications. In *Multitemporal Remote Sensing*; Springer: New York, NY, USA, 2016; pp. 145–176. [[CrossRef](#)]
28. Lanari, R.; Lundgren, P.; Manzo, M.; Casu, F. Satellite radar interferometry time series analysis of surface deformation for Los Angeles, California. *Geophys. Res. Lett.* **2004**, *31*. [[CrossRef](#)]
29. Watson, K.M.; Bock, Y.; Sandwell, D.T. Satellite interferometric observations of displacements associated with seasonal groundwater in the Los Angeles basin. *J. Geophys. Res.-Sol. Earth* **2002**, *107*. [[CrossRef](#)]
30. Zhang, L.; Lu, Z.; Ding, X.; Jung, H.S.; Feng, G.; Lee, C.W. Mapping ground surface deformation using temporarily coherent point SAR interferometry: Application to Los Angeles Basin. *Remote Sens. Environ.* **2012**, *117*, 429–439. [[CrossRef](#)]
31. Borchers, J.W.; Carpenter, M.; Grabert, V.; Dalgish, B.; Cannon, D. Land subsidence from groundwater use in California. In *California Water Foundation Full Report of Findings*; California Water Foundation: Sacramento, CA, USA, 2014; p. 151.
32. Khorrami, M.; Hatami, M.; Alizadeh, B.; Khorrami, H.; Rahgozar, P.; Flood, I. Impact of Ground Subsidence on Groundwater Quality: A Case Study in Los Angeles, California. In *Proceedings of the 2019 ASCE International Conference on Computing in Civil Engineering*, Atlanta, GA, USA, 17–19 June 2019. (In Press)

33. Nikvar Hassani, A.; Katibeh, H.; Farhadian, H. Numerical analysis of steady-state groundwater inflow into Tabriz line 2 metro tunnel, northwestern Iran, with special consideration of model dimensions. *Bull. Eng. Geol. Environ.* **2016**, *75*, 1617–1627. [[CrossRef](#)]
34. Rowe, R.K.; Lee, K.M. Subsidence owing to tunnelling. II. Evaluation of a prediction technique: Reply. *Can. Geotech. J.* **1994**, *31*, 467–469. [[CrossRef](#)]
35. Sharma, J.R.; Najafi, M.; Marshall, D.; Kaushal, V.; Hatami, M. Development of A Model For Estimation of Buried Large Diameter Thin-walled Steel Pipe Deflection Due To External Loads “In Press”. *J. Pipeline Syst. Eng.* **2019**. [[CrossRef](#)]
36. Hatami, M.; Ameri Siahooei, E. Examines criteria applicable in the optimal location new cities, with approach for sustainable urban development. *Middle-East J. Sci. Res.* **2013**, *14*, 734–743.
37. Riding, K.A.; Peterman, R.J.; Guthrie, S.; Brueseke, M.; Mosavi, H.; Daily, K.; Risovi-Hendrickson, W. Environmental and Track Factors That Contribute to Abrasion Damage. In Proceedings of the 2018 Joint Rail Conference, Pittsburgh, PA, USA, 18–20 April 2018.
38. Shi, Y.J.; Li, M.G.; Chen, J.J.; Wang, J.H. Long-Term Settlement Behavior of a Highway in Land Subsidence Area. *J. Perform. Constr. Fac.* **2018**, *32*. [[CrossRef](#)]
39. Lahijanian, B.; Zarandi, M.F.; Farahani, F.V. Double coverage ambulance location modeling using fuzzy traveling time. In Proceedings of the Fuzzy Information Processing Society (NAFIPS), 2016 Annual Conference of the North American, El Paso, TX, USA, 31 October–4 November 2016; pp. 1–6.
40. Argus, D.F.; Heflin, M.B.; Peltzer, G.; Crampé, F.; Webb, F.H. Interseismic strain accumulation and anthropogenic motion in metropolitan Los Angeles. *J. Geophys. Res.-Sol. Earth* **2005**, *110*. [[CrossRef](#)]
41. Gens, R.; Van Genderen, J.L. Review Article SAR interferometry—Issues, techniques, applications. *Int. J. Remote Sens.* **1996**, *17*, 1803–1835. [[CrossRef](#)]
42. Klees, R.; Massonnet, D. Deformation measurements using SAR interferometry: potential and limitations. *Geologie en Mijnbouw* **1998**, *77*, 161–176. [[CrossRef](#)]
43. Smith, L.C. Emerging applications of interferometric synthetic aperture radar (InSAR) in geomorphology and hydrology. *Ann. Assoc. Am. Geogr.* **2002**, *92*, 385–398. [[CrossRef](#)]
44. Alsdorf, D.E.; Melack, J.M.; Dunne, T.; Mertes, L.A.; Hess, L.L.; Smith, L.C. Interferometric radar measurements of water level changes on the Amazon flood plain. *Nature* **2000**, *404*, 174. [[CrossRef](#)]
45. Peduto, D.; Huber, M.; Speranza, G.; van Ruijven, J.; Cascini, L. DInSAR data assimilation for settlement prediction: case study of a railway embankment in the Netherlands. *Can. Geotech. J.* **2016**, *54*, 502–517. [[CrossRef](#)]
46. Daghighi, A.; Nahvi, A.; Kim, U. Optimal Cultivation Pattern to Increase Revenue and Reduce Water Use: Application of Linear Programming to Arjan Plain in Fars Province. *Agriculture* **2017**, *7*, 73. [[CrossRef](#)]
47. Hooper, A.; Bekaert, D.; Spaans, K.; Arkan, M. Recent advances in SAR interferometry time series analysis for measuring crustal deformation. *Tectonophysics* **2012**, *514*, 1–13. [[CrossRef](#)]
48. Bayer, B.; Simoni, A.; Schmidt, D.; Bertello, L. Using advanced InSAR techniques to monitor landslide deformations induced by tunneling in the Northern Apennines, Italy. *Eng. Geol.* **2017**, *226*, 20–32. [[CrossRef](#)]
49. Shafieardekani, M.; Hatami, M. Forecasting Land Use Change in suburb by using Time series and Spatial Approach; Evidence from Intermediate Cities of Iran. *Eur. J. Sci. Res.* **2013**, *116*, 199–208.
50. Perissin, D.; Wang, Z.; Lin, H. Shanghai subway tunnels and highways monitoring through Cosmo-SkyMed Persistent Scatterers. *ISPRS J. Photogr.* **2012**, *73*, 58–67. [[CrossRef](#)]
51. Lundgren, P.; Hetland, E.A.; Liu, Z.; Fielding, E.J. Southern San Andreas—San Jacinto fault system slip rates estimated from earthquake cycle models constrained by GPS and interferometric synthetic aperture radar observations. *J. Geophys. Res.-Sol. Earth* **2009**, *114*. [[CrossRef](#)]
52. Wei, M.; Sandwell, D.; Smith-Konter, B. Optimal combination of InSAR and GPS for measuring interseismic crustal deformation. *Adv. Space Res.* **2010**, *46*, 236–249. [[CrossRef](#)]
53. Bawden, G.W.; Thatcher, W.; Stein, R.S.; Hudnut, K.W.; Peltzer, G. Tectonic contraction across Los Angeles after removal of groundwater pumping effects. *Nature* **2001**, *412*, 812. [[CrossRef](#)] [[PubMed](#)]
54. Riel, B.; Simons, M.; Ponti, D.; Agram, P.; Jolivet, R. Quantifying ground deformation in the Los Angeles and Santa Ana Coastal Basins due to groundwater withdrawal. *Water Resour. Res.* **2018**, *54*, 3557–3582. [[CrossRef](#)]
55. Sharma, P.; Jones, C.E.; Dudas, J.; Bawden, G.W.; Deverel, S. Monitoring of subsidence with UAVSAR on Sherman Island in California’s Sacramento–San Joaquin Delta. *Remote Sens. Environ.* **2016**, *181*, 218–236. [[CrossRef](#)]

56. Jeanne, P.; Farr, T.G.; Rutqvist, J.; Vasco, D.W. Role of agricultural activity on land subsidence in the San Joaquin Valley, California. *J. Hydrol.* **2019**, *569*, 462–469. [[CrossRef](#)]
57. Tapete, D.; Morelli, S.; Fanti, R.; Casagli, N. Localising deformation along the elevation of linear structures: An experiment with space-borne InSAR and RTK GPS on the Roman Aqueducts in Rome, Italy. *Appl. Geogr.* **2015**, *58*, 65–83. [[CrossRef](#)]
58. Bekaert, D.; Hamlington, B.; Buzzanga, B.; Jones, C. Spaceborne Synthetic Aperture Radar Survey of Subsidence in Hampton Roads, Virginia (USA). *Sci. Rep.-UK* **2017**, *7*, 14752. [[CrossRef](#)] [[PubMed](#)]
59. Rabus, B.; Eppler, J.; Sharma, J.; Busler, J. Tunnel monitoring with an advanced InSAR technique. In Proceedings of the Radar Sensor Technology XVI, Baltimore, MD, USA, 23–25 April 2012; p. 83611F.
60. Nahvi, A.; Daghighi, A.; Nazif, S. The environmental impact assessment of drainage systems: a case study of the Karun river sugarcane development project. *Arch. Agron. Soil Sci.* **2018**, *64*, 185–195. [[CrossRef](#)]
61. Davidson, M.; Attema, E.; Rommen, B.; Floury, N.; Partricio, L.; Levrini, G. ESA sentinel-1 SAR mission concept. In Proceedings of the EUSAR, Dresden, Germany, 16–18 May 2006.
62. Metro. Webpage of Sepulveda Transit Corridor Project. Available online: <https://www.metro.net/projects/sepulvedacorridor/> (accessed on 5 August 2018).
63. Ferretti, A.; Prati, C.; Rocca, F. Permanent scatterers in SAR interferometry. *IEEE Trans. Geosci. Remote* **2001**, *39*, 8–20. [[CrossRef](#)]
64. Canaslan Comut, F.; Ustun, A.; Lazecky, M.; Perissin, D. Capability of Detecting Rapid Subsidence with COSMO SKYMED and Sentinel-1 Dataset over Konya City. In Proceedings of the Living Planet Symposium, Prague, Czech Republic, 9–13 May 2016; p. 295.
65. Perrone, G.; Morelli, M.; Piana, F.; Fioraso, G.; Nicolò, G.; Mallen, L.; Cadoppi, P.; Balestro, G.; Tallone, S. Current tectonic activity and differential uplift along the Cottian Alps/Po Plain boundary (NW Italy) as derived by PS-InSAR data. *J. Geodyn.* **2013**, *66*, 65–78. [[CrossRef](#)]
66. Hanssen, R.F. *Radar Interferometry: Data Interpretation and Error Analysis*; Springer Science & Business Media: New York, NY, USA, 2001; Volume 2.
67. Ferretti, A.; Prati, C.; Rocca, F. Nonlinear subsidence rate estimation using permanent scatterers in differential SAR interferometry. *IEEE Trans. Geosci. Remote* **2000**, *38*, 2202–2212. [[CrossRef](#)]
68. Colesanti, C.; Ferretti, A.; Novali, F.; Prati, C.; Rocca, F. SAR monitoring of progressive and seasonal ground deformation using the permanent scatterers technique. *IEEE Trans. Geosci. Remote* **2003**, *41*, 1685–1701. [[CrossRef](#)]
69. Murray, J.R.; Svarc, J. Global Positioning System data collection, processing, and analysis conducted by the US Geological Survey Earthquake Hazards Program. *Seismol. Res. Lett.* **2017**, *88*, 916–925. [[CrossRef](#)]
70. Metro. *Final Compendium Report of Sepulveda Transit Corridor: Appendix B, Geotechnical Evaluation Memorandum*; The Los Angeles County Metropolitan Transportation Authority: Los Angeles, CA, USA, 2012.
71. CGS. *California Geological Survey: Seismic Hazard Zones, Beverly Hills Quadrangle, Official Map*; CGS: Sacramento, CA, USA, 1999.
72. CGS. *California Geological Survey: Seismic Hazard Zone Report for the Van Nuys 7.5-Minute Quadrangle*; CGS: Sacramento, CA, USA, 1997.
73. CGS. *California Geological Survey: Seismic Hazard Zone Report for the Venice 7.5-Minute Quadrangle*; CGS: Sacramento, CA, USA, 1998.
74. California's Groundwater. *Groundwater Basin Number: 4-12, San Fernando Valley Groundwater Basin, Bulletin 118*; California's Groundwater, 2004. Available online: https://www.bhusd.org/pdf/seismic_reports/___36_Leighton%20El%20Rodeo%20Geohazards%20Report_3-2-15.pdf (accessed on 8 September 2018).
75. California's Groundwater. *Groundwater Basin Number: 4-11.01, Coastal Plain of Los Angeles Groundwater Basin, Santa Monica Subbasin, Bulletin 118*; California's Groundwater, 2004. Available online: <http://www.water.ca.gov/groundwater/bulletin118/basindescriptions/4-11.01.pdf> (accessed on 12 September 2018).
76. LADWP. *Feasibility Report for Development of Groundwater Resources in the Santa Monica and Hollywood Basins*; LADWP: Los Angeles, CA, USA, 2011.
77. Poland, J.F.; Garrett, A.A.; Sinnott, A. *Geology, Hydrology, and Chemical Character of Ground Waters in the Torrance-Santa Monica Area, California*; US Government Printing Office: Washington, DC, USA, 1959.
78. Norris, R.M.; Webb, R.W. *Geology of California*; John Wiley & Sons Inc.: Hoboken, NJ, USA, 1990.
79. Ninyo & Moore Geotechnical & Environmental Sciences Consultants. *Geotechnical Evaluation Sepulveda Feeder Interconnection Project Culver City, California*. 2009. Available online: <https://dpw.lacounty>

- [gov/www/wwd/web/Documents/Reports/Sepulveda%20Feeder%20Service%20Connection.pdf](http://www.wwd/web/Documents/Reports/Sepulveda%20Feeder%20Service%20Connection.pdf) (accessed on 7 August 2018).
80. Shannon & Wilson, Inc. Geology and Soil Discipline Report: the Academy Museum of Motion Picture, Los Angeles. 2014. Available online: https://planning.lacity.org/eir/AcademyMuse_MotionPictures/DEIR/DEIR/Technical_Appendices/Appendix_H-1_Methane_Report.pdf (accessed on 14 June 2018).
 81. Geotechnologies, Inc. Geotechnical Report: Geotechnical Engineering Investigation Proposed Mixed-Use Development 6001–6059 Van Nuys Boulevard, Van Nuys, California. 2015. Available online: <https://planning.lacity.org/eir/nops/6001VanNuys/appendixa.pdf> (accessed on May 2018).
 82. Leighton Consulting, Inc. Geohazard Report: El Rodeo K-8 School 605 Whittier Drive, Beverly Hills, Los Angeles. 2015. Available online: https://www.bhusd.org/pdf/seismic_reports/___36_Leighton%20El%20Rodeo%20Geohazards%20Report_3-2-15.pdf (accessed on 16 June 2018).
 83. Ninyo & Moore Geotechnical & Environmental Sciences Consultants. Runway 25R Reconstruction Project: Runway 25R-7L Improvements, Los Angeles International Airport (LAX), California. 2017. Available online: <http://www.labavn.org/contracts/documents/81/30368/Runway%2025R%20Reconstruction%20RFB.pdf> (accessed on 19 April 2018).
 84. SCS Engineers, Inc. Groundwater Monitoring Program, Inglewood Field. 2018. Available online: <https://inglewoodoilfield.com/csd-related-plans> (accessed on 2 April 2018).
 85. Hodgkinson, K.M.; Stein, R.S.; Hudnut, K.W.; Satalich, J.; Richards, J.H. *Damage and Restoration of Geodetic Infrastructure Caused by the 1994 Northridge, California, Earthquake*; US Geological Survey: Reston, VA, USA, 1996.
 86. Martz, P. Asymmetrical Subsidence Resulting from Material and Fluid Extraction. 2009. Available online: <https://open.library.ubc.ca/media/download/pdf/52966/1.0053573/1> (accessed on 23 May 2018).
 87. Jozaghi, A.; Alizadeh, B.; Hatami, M.; Flood, I.; Khorrami, M.; Khodaei, N.; Ghasemi Tousi, E. A Comparative Study of the AHP and TOPSIS Techniques for Dam Site Selection Using GIS: A Case Study of Sistan and Baluchestan Province, Iran. *Geosciences* **2018**, *8*, 494. [[CrossRef](#)]
 88. Hatami, M.; Shafieardekani, M. The Effect of Industrialization on Land Use Changes; Evidence from Intermediate Cities of Iran. *Int. J. Curr. Life Sci.* **2014**, *4*, 11899–11902.
 89. Desir, G.; Gutiérrez, F.; Merino, J.; Carbonel, D.; Benito-Calvo, A.; Guerrero, J.; Fabregat, I. Rapid subsidence in damaging sinkholes: Measurement by high-precision leveling and the role of salt dissolution. *Geomorphology* **2018**, *303*, 393–409. [[CrossRef](#)]



© 2019 by the authors. Licensee MDPI, Basel, Switzerland. This article is an open access article distributed under the terms and conditions of the Creative Commons Attribution (CC BY) license (<http://creativecommons.org/licenses/by/4.0/>).